Boletim Técnico da Escola Politécnica da USP
Departamento de Engenharia Eletrônica

ISSN 1413-2206
BT/PEE/9913

Polarization Effects on the Raman and Photoluminescence Spectra of Porous Silicon Layers

Walter Jaimes Salcedo
Francisco Javier Ramirez Fernandez

São Paulo – 1999

FICHA CATALOGRÁFICA

Jaimes Salcedo, Walter
Polarization effects on the Raman and photoluminescence spectra of porous silicon layers / W. Jaimes Salcedo, F.J. Ramirez Fernandez. -- São Paulo : EPUSP, 1999.
21 p. -- (Boletim Técnico da Escola Politécnica da USP, Departamento de Engenharia Eletrônica, BT/PEE/9913)

1. Silico poroso 2. Fotoluminescência 3. Nanoestruturas I. Ramirez Fernandez, Francisco Javier II. Universidade de São Paulo. Escola Politécnica. Departamento de Engenharia Eletrônica III. Título IV. Série
ISSN 1413-2206 CDD 620.193
535.355
620.5

POLARIZATION EFFECTS ON THE RAMAN AND PHOTOLUMINESCENCE SPECTRA OF POROUS SILICON LAYERS

Walter Jaimes Salcedo*, Francisco J. Ramirez Fernandez

Laboratório de Microeletrônica da Escola Politécnica da Universidade de São Paulo. C.P.61548, 05424 - 970, São Paulo, SP, Brazil

and

Joel C.Rubim

Instituto de Química da Universidade de São Paulo, Av.Prof. Lineu Prestes, 748, 05508-900, São Paulo, SP, Brazil

Abstract

The effect of different polarization orientation of the excitation source on the Raman and photoluminescence (PL) spectra of a porous silicon (PS) layer within two different micro-regions has been investigated. Two micro regions (2 μm) along the (100) direction have been investigated, close to the c-Si – PS layer interface and the PS layer – air interface. The Raman depolarization factors obtained in the 100 - 1200 cm^{-1} phonon spectra of this two micro regions have shown that the anisotropy presented by the PS layer is similar to that presented by the c-Si (100). Large differences in the Raman line widths and different emission maxima in the PL spectra have been observed for the two micro regions. These results have been interpreted as the PS layer being inhomogeneous along the (100) direction. These effects were discussed from a critical point of view by taking into account quantum confinement and chemical composition of the nano-crystallite surface since the SiH_2 stretching mode was also observed in the Raman spectra. Excitation with different polarization causes a shift on the emission maxima. This shift has been assigned to a polarization dichroism caused by a breakdown on the degeneracy as the nanocrystallites having a reduced symmetry in relation to c-Si. The results here presented strongly supports the hypothesis that the luminescence presented by the PS layer is due to the presence of Si-based compounds on the surface of Si nanocrystallites.

INTRODUCTION

Silicon has been the dominant material in microelectronics for several decades. The technology and fabrication of Si-based electronic devices had been developed and refined in its ways and commercial applications. However, crystalline silicon is an indirect semiconductor with a very low efficiency for radiactive recombination at room temperature. Indeed crystalline silicon (c-Si) has never been a good candidate for active optoelectronic devices. This is true for commonly available bulk Si samples.

About six years ago Caham[1] reported the observation of a strong photoluminescence (PL) in porous Si (PS) under UV illumination at 300K. Independently, Lehmann and Gosele[2] observed a pronounced shift of the fundamental absorption edge of self-supporting porous silicon layer.

In 1950, porous Si was obtained for the first time during the electrochemical polishing (anodization) of a c-Si sample in hydrofluoric acid (HF) containing electrolytes[3]. However, only 40 years later it was realised that this material shows unexpected strong room temperature luminescence in the visible range. Even though many groups have confirmed the existence of strong luminescence in PS layers, the origin and mechanism of the luminescence remain controversial[4-9] (Note: see for instance the conclusions of the authors in refs [8] and [9]).

Information about structure, bonding and disorder on PS layers can be obtained by Raman spectroscopy since the frequencies and relative intensities of vibrations and phonons are dependent on structure and chemical environment, and depolarization factors are dependent on the structure and level of disorder. Many researchers report polarization effects in the Raman spectra of PS layers[10-13] , but in general the results are controversial. However, literature has ignored the anisotropy behaviour of second order Raman scattering in PS except for the work of Taning et al[12].

The photoluminescence spectra of PS layers present a strong dependence on the nature of the PS substrate[9] . Therefore the PL spectra of PS should contain information regarding to the structure and bonding on PS layers. Since PL and Raman spectroscopies are governed by different selection rules it is believed that a simultaneous study on the polarization effects on Raman and PL spectra of PS layers can provide a better understanding of structural, bonding and anysotropic properties of this material.

EXPERIMENTAL

Porous silicon (PS) was prepared by the electrochemical anodization method using a p-Si (100) oriented wafer with a resistivity of 10-20 Ωcm. Before anodization, the back side of the wafer was doped with Boron at 925°C in a N_2, O_2, and BBr_3 environment. Ohmic contact was made by evaporating an Aluminium film (0.5 μm) and by subsequent annealing in N_2 environment at 450°C. The PS layer was then obtained by applying constant d.c. currents of 20 and 40 mA/cm^2 in steps of 5 minutes for a total anodization time of 20 minutes. The anodization was performed in a 41% wt. HF aqueous solution. The electrochemical system used in the anodization process was a HP E3631A triple output DC power supply and a HP 34401A multimeter. The thickness of the PS layer is ca. 20 μm. The sample so prepared was maintained at room atmosphere for 6 months prior to the measurements described in this work.

The Raman and photoluminescence (PL) spectra were obtained on a Renishaw Raman system 3000 equipped with CCD detector and an Olympus BH-2 microscope . The measurements were made in the back scattering geometry using a 80x microscope objective to focus the laser beam on the sample. The area of the laser spot on the sample using the 80x objective is ca. 2μm. The laser source was the 488 nm line of an air cooled Ar^+ laser from Ohmnichrome. The laser power measured at the focus of the 80x objective was less than 50 μW. All spectra were recorded at room temperature (ca. 20 °C). It is worth to mention that the Renishaw instrument is confocal. The spectral resolution was ca. 4 cm^{-1} and the frequency precision ± 1 cm^{-1} calibrated against the 520 cm^{-1} LO phonon of c-Si.

Polarization measurements were performed using an analyser after the notch filters and a quarter wave plate was set between the analyser and the entrance slit of the monochromator to correct the grating response for different polarizations of the scattered light. This experimental setup for polarization measurements was tested with CCl_4. The experimental arrangement is described as follows (see Figure 1):

i) Uncleaved sample: The sample was placed under the microscope in order that the excited and scattered beams have the direction normal to the surface, that is, the same direction of the Z axis, here assumed as the (100) direction of the c-Si single crystal. The incident laser light is polarized parallel to the surface in the Y direction. The scattered radiation was then recorded with a analyser set at 0 and 90 degrees corresponding to the $Z(YY)\bar{Z}$ ($E_i//E_s$) and $Z(YX)\bar{Z}$ ($E_i \perp E_s$) configurations, respectively (E_i and E_s are the electric fields of the incident and scattered photons). After that, the sample was rotated by 90 degrees around the Z axis and

Raman phonon spectra were recorded with the analyzer at 90 and 0 degrees, corresponding to the $Z(XX)\bar{Z}$ ($E_i//E_s$) and $Z(XY)\bar{Z}$ ($E_i \perp E_s$) configurations, respectively.

ii) Cleaved sample: The experimental arrangement was so that the incident and scattered beams were normal to the cleaved surface. In this arrangement the $\bar{Z}$ direction is the (011) crystal orientation which is normal to the Y axis, assumed as the (100) crystal orientation. The direction of the cleavage is the X direction. The laser beam was polarized parallel to the Y direction and the spectra were recorded with the analyzer at 0 and 90 degrees corresponding to the $Z(YY)\bar{Z}$ ($E_i//E_s$) and $Z(YX)\bar{Z}$ ($E_i \perp E_s$) configurations, respectively. After that, the sample was rotated by 90 degrees around the Z axis and Raman phonon spectra were recorded with the analyser at 90 and 0 degrees, corresponding to the $Z(XX)\bar{Z}$ ($E_i//E_s$) and $Z(XY)\bar{Z}$ ($E_i \perp E_s$) configurations, respectively. It is worth mentioning that for the cleaved sample two regions in the PS film were investigated, a region close to the PS layer surface (labelled Region I) and another one close to the c-Si – PS layer interface (labelled Region II). Figure 2 shows an optical microscopic image of the cleaved sample indicating the two investigated regions.

RESULTS

The c-Si has the same crystal symmetry of diamond, i.e., it belongs to the O^7_h (*Fd3m*) space group. Therefore it has only one first-order Raman active phonon of symmetry $\Gamma_{25'}$ located at the Brillouin-zone centre. The Raman tensor in c-Si contains the Γ_1, Γ_{12}, and $\Gamma_{25'}$ irreducible representations. Therefore, using the experimental arrangements described in Figure 1 for the cleaved and uncleaved samples, the off diagonal elements, XY and YX, will be allowed (A) while the diagonal elements, XX and YY, will be forbidden (F). The Raman spectra of the uncleaved sample recorded for the different scattering configurations are displayed in Figure 3. Figures 4 and 5 present the Raman phonon spectra at the indicated scattering configurations in the uncleaved sample at regions I and II, respectively. The inset of Figure 5 shows the Raman spectrum at the region II in the Si-H stretching region.

The photoluminescence spectra were recorded using the same optical configuration used to record the Raman spectra and the same labels were used to indicate the scattering configuration in order to maintain a geometry correspondence, i.e., the PL spectra recorded with $E_i//E_e$ (E_e is the electric field of the emitted photons) is labelled as "F" and the PL spectra obtained with $E_i \perp E_e$ is labelled as "A". The PL spectra at regions I and II, with different polarization arrangements are shown in the Figures 6 and 7, respectively.

DISCUSSION

The 510 cm^{-1} line observed in all investigated configurations can be assigned to the downshifted first order Raman phonon (LO) of c-Si. The other features, at 636 cm^{-1} and 970 cm^{-1} may be due to the second order Raman effect or to some phonon scattered at the PS surface. Table I shows the Raman shift and the full width at half maximum (FWHM) values for the c-Si LO phonon and those for the Raman feature observed at ca. 510 cm^{-1} in the spectra of Figures 3 to 5. Note that the first order phonon signal of the PS layer has a FWHM value much larger than that observed for c-Si. Note also that the FWHM values for the uncleaved sample at F (or F') configuration is almost twice that of A (or A') configuration.

The shift and broadening of the Si-Si Raman line has been explained as a result of phonon confinement in silicon nanocrystals inside the PS layer produced during electrochemical etching[13-17]. The effects of spatial confinement of phonons in small Si particles has been studied theoretically and experimentally[18,19]. The breakdown of the K-selection rule leads to a broadening of the optical phonon. This broadening is correlated with the size and shape of the small particles. In the quantum confinement model the phonon wave function is seen as a superposition of non confined phonon wave functions multiplied by a weighting amplitude function. This amplitude is a function of the wave vector within the first Brillouin zone. Therefore, it depends on the phonon scattering direction[18,19].

The corresponding phonon confinement function can be expressed in a Fourier series and the Raman spectrum is then described by integrating over phonon Lorentzians weighted by the square of the Fourier transform of the confinement function. The choice of the weighting function is determined mainly by physical assumptions[19]. In most cases a Gaussian is used as the weighting function. However, the spectra obtained in many studies[20,21] do not match the theoretical predictions. These discrepancies can not be eliminated by the choice of nanocrystallite shape. The assumption of the phonon amplitude being exactly equal to zero, i.e. a "sine" weighting function at the boundary does not change significantly the relationship between the peak shift and line width (FHMW) and leads mainly to a decrease in the diameter of spherical nanocrystallites[22-25].

The PS sample investigated in this work shows a downshift, $\Delta\omega$, of ca. 10-11 cm^{-1} for the first order Raman line relative to the LO phonon of the c-Si. Using a quantum confinement model as described above, the estimated average size of the crystallites in the PS layer is ca. 3.1 nm. This particle size corresponds to a FWHM value of 15 cm^{-1} while our measurements show FWHM values around 40 cm^{-1}, i.e., a large difference between theoretical predictions and experiment.

Some attention should be given to the comparison of the spectral lines observed in our experiments with Raman lines observed in other Si containing materials that present photoluminescence properties comparable to that of PS. The Polysilane, for instance, prepared through the reduction of dichlorosilane (SiH_2Cl_2) with granular Lithium[26], shows a Raman peak centred at 480 cm^{-1} with a FWHM of ca. 62 cm^{-1}. This peak is assigned to Si-Si chain backbone vibrations (ω_{LO} mode)[26]. On the other hand, polysilane shows other Raman features at 636 cm^{-1} and 909 cm^{-1} with FWHM of ca. 106 cm^{-1} and 45 cm^{-1}, respectively. These peaks have been assigned to the SiH_2 rocking and bending modes, respectively[26]. Similar peaks are also observed in the Raman spectra of PS. However, the 630 cm^{-1} and 970 cm^{-1} lines observed in Figures 3-5 present FWHM values of ca. 54 cm^{-1} and 197 cm^{-1}, respectively.

Another interesting material, with the same PL behaviour as that of PS layers, is the Siloxene[27-30]. In this case, the 515 cm^{-1} line is assigned to the Si-Si vibration in the plane of Siloxene. The feature at 490 cm^{-1} (appearing as a shoulder in the Raman spectra) is assigned to a Si-Si ring vibration in Siloxene. The PL effect in Siloxene is attributed to the Si-Si ring structure. However, for the Siloxene[29], the peaks at 630 cm^{-1} and 970 cm^{-1} are not reported despite the existence of the lines at 2130 cm^{-1} and 2250 cm^{-1} assigned to SiH_2 stretching modes (see the inset of Figure 5).

Taking into account the above data for different Si containing materials it is not possible to assign the 630 cm^{-1} line reported in this work only to the SiH_2 bending modes . It is well known that the LO(X) +TA(X) mode in c-Si[12,31] lies at 636 cm^{-1}. The intensity of this mode at room temperature is close to zero. We suggest that the 630 cm^{-1} line in PS is a consequence of the combination of the LO(X) and TA(X) modes. The enhancement of this mode in the PS is due to the relaxation of selection rules and surface assistance as it was suggested by Tanino et al[12]. However, the contribution of a SiH_2 bending mode to this Raman line should not be disregarded since we observe the SiH_2 stretching mode in the Raman spectra of the PS layer (see the inset of Figure 5(a)). The same explanation given above for the observation of the 630 cm^{-1} feature can be used to explain the broadening of the line at 970 cm^{-1} in the Raman spectra of PS relative to the same line on the spectra of c-Si. Therefore, the broad feature at 970 cm^{-1} is the contribution of second-order Raman scattering, as in c-Si, and the SiH_2 rocking mode of hydrogenated silicon species[32].

At this point it is difficult to say if the quantum confinement effect or the surface effect plays the major role in the PL features observed in the PS layers. In this sense it is necessary to evaluate the selection rules in more detail.

From Figures 3, 4, and 5 it can be seen that the lines of second order Raman scattering (630 and 970 cm^{-1}) in A configuration are more intense for the cleaved sample than for uncleaved one. In the F configuration all these lines have their intensities within the noise level. This fact reveals a strong anisotropy for these lines.

To analyse the first order Raman line anisotropy, the depolarization factor, ρ, is defined as $\rho = I_F/I_A$, i.e., the ratio of the Raman intensities at $E_i // E_s$ and $E_i \perp E_s$. Table II presents the depolarization factors for the experiments described in this paper and those reported by other research groups. The accuracy of the depolarization ratios were checked by the determination of the depolarization ratios for the 314 and 460 cm^{-1} lines of CCl_4, which were 0.71 and 0.016, respectively.

Table II shows a large dispersion for ρ values. However it is worth to mention that our sample present low values of ρ which reminds those of the c-Si. In order to compare these values we considered an extreme case for Si, i.e., Si crystallites randomly oriented, in analogy with liquids or powders[33]. In the Raman scattering configuration we used the depolarization ratio expressed as:

$$\rho = \left(\frac{A_{XX}}{A_{YY}} \right)^2$$

where X, Y, Z represent the laboratory coordinates system and x, y, z that of the crystal unit cell. A_{IJ} is the Raman tensor component of the fluid or powder as a whole in the coordinate system XYZ which is fixed in the laboratory relative to scattering experiment. On the other hand a_{ij} is the Raman tensor component of the N oriented particles of the scatter in a xyz coordinate system.

If the Si crystallites are randomly oriented, the A_{ij} value is determined by averaging over all orientations of crystallites. At this condition the ρ value is c.a. 1.33 that is very different from the ρ value experimentally obtained for our PS sample. Finally, it can be observed that the depolarization values for our PS sample are more close to those of c-Si, suggesting that our PS sample has a c-Si-skeleton like structure.

The PL spectra were recorded at regions I and II of the cleaved sample. The labels A and F have the same meaning as described for the Raman spectra. Table III summarises the photoluminescence results. The depolarization factor is defined as in the Raman experiments.

If we assume that the Si-Si rings (present in Siloxene) are responsible for the PL effect in the PS, a higher intensity for PL emission should be correlated with a higher density of Si-Si rings. Therefore, one would expect a broadening of the Raman phonons in the 450-520 cm^{-1} spectral region. In other words, the contribution of the Si-Si ring stretching at 490 cm^{-1} should be more intense. Based on these considerations we assign the larger FWHM of the first order phonon spectrum at region I (in relation to region II) to a higher density of Si-Si rings (or Siloxene) on the PS layer. Despite this correspondence, it is not possible to say that the presence of Si-Si rings as in Siloxene is the origin of the PL in PS layer once the 630 cm^{-1} Raman feature is not observed in the Siloxene spectra but it is observed in the PS layer as stated above.

From Table III one can see that the maximum of PL emission at region I is blue shifted in relation to region II. It is not possible to correlate this shift with the shift of the first order Raman peak because in the later the shift is close to the experimental error (2 cm^{-1}). According to the quantum confinement model for PL emission in PS layers, the peak of emission is related to the size of the nano-crystallite. As smaller is the crystallite as more shifted to the blue is the PL emission peak. Therefore, one could say that the nano-crystallites at region I are smaller than those at region II. On the other hand the calculations based on quantum confinement for both regions have shown that there is no appreciable difference on the crystallite dimensions at regions I and II.

Kovalev et al.[34] have also investigated the polarization effects on PS layers. These authors have also used an objective microscope to focus the laser beam on their sample. The PS film they investigated was a (100) oriented PS layer generated by anodization on a c-Si(100). The film thickness was 20 μm and the laser spot on the sample had a diameter of 10 μm. The linear polarization factor as described in Table III obtained by these author when the electric field of the exciting radiation was parallel and perpendicular to the (100) direction were ca. 0.2 and –0.08, respectively. For laser electric field polarized perpendicular to the (100) direction and using their definition we have obtained linear polarization factors of 0.25 and –0.08 for regions I and II, respectively (see Table III). These results suggest that the anisotropic properties of the PS film is not the same along the (100) direction in the PS layer. Probably, Kovalev and co-workers[34] have not observed this film inhomogeneity because they have used a laser spot five times larger than we used.

It is worth to mention that in both regions the PL emission maximum presents a red shift (ca. 130 cm^{-1}) when changing the polarization from parallel to perpendicular. This shift on the emission maximum with the polarization configuration was not observed by Kovalev et al.[34]

Kovalev et al.[34] interpreted their results as the nano-crystallites having their major axis oriented along the (100) direction. On the other hand, our results show that there is an inhomogeneous anisotropy along the PS (100) direction. This anisotropy can not be explained in terms of changes in the crystallite orientation within the PS layer. As the Raman results show (see Table 2), the contribution of the Si-Si stretching at region I is stronger than at region II, suggesting that the chemical composition of the crystallites are not constant along the (100) direction. These facts besides the shift of the emission maxima with the change in the laser polarization led us to conclude that the PL emission presented by the PS layer here investigated has its origin on the presence of different excited states generated by the presence of Si-based surface composites, like Siloxene and parent compounds as described by Gole and Dixon [9]. Once the emitted photon is confined within the Si nano-crystallite, the observation of its emission depends now on the nano-crystallite structure. Therefore, if the symmetry of the crystallite is reduced in relation to the c-Si (having states with high degeneracy), one should expect a breakdown in the degenereacy and new emission bands would be observed. Indeed, we have observed for other PS samples more than one component in the PL spectra at 700 nm spectral region and their relative intensities have changed with the laser polarization. This observation is under further investigation in our laboratory.

Conclusion

Contrary to other Raman polarization studies[10-12], the results here presented show that the PS layer here investigated has an anisotropic behaviour similar to that of c-Si. This fact suggests a c-Si-skeleton as the structure for the porous silicon. A well structured nano-crystal network can also be inferred from the polarization measurements on PL emission.

The Raman and PL measurements with polarized light show that there is an inhomogeneous behaviour of the anisotropy along the (100) direction in the PS layer. This inhomogeneity has been assigned to different chemical compositions of the nano-crystallite surface for crystallites within the region I (close to the PS/air interface) and region II (close to the c-Si/PS interface).

The PL emission band of the PS layer presents a polarization dichroism, i.e. a shift on its maximum as the polarization of the excitation source changes. This polarization dichroism is tentatively assigned to a symmetry reduction of the nano-crystallites in relation to the c-Si, with a breakdown in the degeneracy.

As far as we know this work reports for the first time the presence of the SiH_2 stretching modes in PS layers as measured by Raman spectroscopy.

REFERENCES

1. L. T. Canham, *Appl. Phys. Lett.* **57**, 1046 (1990)

2. V. Lehmann and U. Gosele, *Appl. Phys. Lett.* **58**, 856 (1991)

3. D. R. Turner, *J. Electrochem. Soc.* **105**, 402 (1958)

4. F. Koch, V. Petrova-Koch and T. Muschik, *J. Lumin.* **57,** 271 (1993).

5. C. Delerue, M. Lannoo and G. Allan, *J. Lumin.* **57**, 249 (1993).

6. J. D. Lockwood, *Sol. Stat. Commun.* **92**, 101, (1994)

7. M. Voos, Ph. Uzan, C. Deilande, and G. Bastard, *Appl. Phys. Lett.* **61**, 1213, (1992).

8. H. Noguchi, T. Kondo and K. Uosaki, *J. Phys. Chem. B*, **101**, 4978 (1997).

9. J.L. Gole and D.A. Dixon, *J. Phys. Chem. B*, **102**, 33 (1998).

10. I. gregora, B. Champagnon, L. Saviot, Y. Monin, *Thin Solid Films*. **255**, 139, (1995).

11. I. Gregora, B. Champagnon, A. Halimaoui, *J. Appl. Phys.* **75**, 3034, (1994).

12. H. Tanino, A. Kupring and H. Deai, *Phys. Rev. B.* **53**, 1937, (1996).

13. S. Guha, P. Steiner, F. Kozlowski, W. Lang, *Thin Solid Films*. **276,** 73 (1996).

14. M. Yong, D. Huang, P. Hao, F. Zhang, X. Hou and X. Wang, *J. Appl. Phys.* **75**, 651, (1994).

15. S. Guha, P. Steiner, W. Lang, *J. Appl. Phys.* **79**, 8664, (1996).

16. C. Jarding, B. Gruzza, E. Vazsonyi, G. Geryley, *Vacuum* **46**, 497, (1995).

17. I. I. Reshina and E. G. Guk, *Semiconductors* **27**, 401, (1993).

18. H. Richter, Z. P. Wang and L. Ley, *Sol. Stat. Commun.* **39**, 739, (1981).

19. I. H. Campbell and P. M. Fauchet, *Sol. Stat. Commun.* **58**, 739, (1986).

20. R. Tsu, H. Shen, and M. Dutta, *Appl. Phys. Lett.* **60**, 112, (1992).

21. J. M. Perez, J. Villalobos, P. Mcneill, J. Prasad, R. Cheek, J. Kelber, S. P. Esterera, P. D. Stevens and R. Glosser, *Appl. Phys. Lett.* **61**, 563, (1992).

22. H. Munder, C. Andrzejok, M. G. Berger, U. Klemrodt, H. Luth, R. Herino and M. Ligeon, *Thin Solid Films* **221**, 27, (1992).

23. G. Mariotto, F. Ziglio, F. L. Freire Jr., *J. Non Cryst. Solids.* **192 & 193**, 253, (1995).

24. G. Mariotto, F. Ziglio, F. L. Freire Jr, *J Appl. Phys.* **78**, 3335, (1995).

25. G. C. John and V. A. Singh, *Phys Rev. B.* **50**, 5329, (1994).

26. P. Vora, S. A. Solin, P. John, *Phys. Rev. B* **29**, 3423, (1984).

27. H. D. Fuschs, M. Sutzmann, M. S. Brandt, M. Resembauer, J. Weber and M. Cardona, *Phys Scrip.* **T45**, 309 (1992).

28. P. Deak, M. Rosembauer, M. Stutzmann, J. Weber, M. S. Brandt, *Phys. Rev. Lett.* **69**, 2531, (1992).

29. D. Fuschs, M. Sutzmann, M. S. Brandt, M. Resembauer, J. Weber A. Breitschewerdt, P. deak and M. Cardona, *Phys. Rev. B.* **48**, 8172, (1993).

30. M. Stutzmann, *Phys. Stat. Sol. (b)*, **192**, 273, (1995).

31. J. L. Berman, *Phys. Rev.* **131**, 1489, (1963).

32. M. H. Brosky, M. Cardona, J. J. Cuomo, *Phys. Rev. B.* **16**(8), 3556 (1977)

33. W. Hayes, R. Loudon, "Sacattering of Light by Crystals". John-Wiley & Sons New York (1978).

34. D. Kovalev, M. Bem Chorin, J. Diener, F. Koch, A. Kux, Al.L. Efros, M. Rosen, N.A. Gippius, S.G. Tikhodeev, *Thin Solid Films*, **276**, 120 (1996).

35. Z. Iqbal, S. Vepiek, A. P. Webb and P. Capezzuto, *Sol. Stat. Commun.* **37**, 993, (1981).

Table I. Raman shifts, intensities and full width at half maximum values for the phonons observed in the Raman spectra of the c-Si (100) and PS sample at the different scattering configurations. Spectral range analysed: 400 – 550 cm^{-1}.

Sample	Wavenumber/cm^{-1}				Intensity/a.u.				FWHM/cm^{-1}			
Configuration	A	F	A'	F'	A	F	A'	F'	A	F	A'	F'
c-Si	520	519	522	519	5778	134	6047	87	7	11	7	11
Uncleaved PS	511		509	511	472	36	492	17	43	76	35	73
PS region I	509		509		1035	144	1613	137	52	33	41	45
PS region II	511	511	513	509	1027	146	1514	138	39	24	34	39

Table II: The depolarization factors as obtained in this work and reported in the literature.

Sample	$\rho = (I_F/I_A)$	$\rho' = (I_{F'}/I_{A'})$
PS (uncleaved)[a]	0.8	0.03
PS (cleaved Region I)[a]	0.12	0.09
PS (cleaved Region II)[a]	0.14	0.09
c-Si(100)[a]	0.02	0.01
PS/Si(100)P^+	2	
Siloxene[b,29]	5	
PS/Si(111)[12]	2 – 0.4	
c-Si (111)[12]	0.3	
PS P^+-Si(100)[13]	1.25	
Randomly oriented μ-crystal of Si[a,b]	1.33	
μ-crystal of Si[35]	2	

[a] this work; [b] calculated

Table III: Emission peak, full width at half maximum (FWHM), intensity, and depolarization fators for the emissions observed in the photoluminescence spectra of the cleaved PS sample at Regions I and II.

	Region I		Region II	
Configuration	F	A	F	A
Peak of emission/eV	1.781	1.762	1.747	1.744
FWHM/eV	0.241	0.222	0.238	0.223
Intensity/a.u.	362120	217730	14260	16873
$\rho = I_F/I_A$	1.66		0.85	
$\rho(l)^* = I_F-I_A/I_F+I_A$	0.25		-0.08	

*$\rho(l) = I_F-I_A/I_F+I_A$ is definition of the linear polarization factor used by Kovalev et al.[34]

Caption to the Figures

Figure 1. Geometry configuration for the uncleaved (a) and cleaved (b) samples using the laboratory coordinates where X is parallel to the entrance slit of the instrument, Y is the observation direction, Z and $\overline{Z}$ are the incident and scattered directions, respectively.

Figure 2. Optical microscopic image of the sample investigated in this work obtained with the 80x objective of a microscope. The labels I and II stand for the different regions of the PS layer.

Figure 3: Raman spectra of the uncleaved sample at different scattering configurations.

Figure 4: Raman spectra for the cleaved sample at region I for different scattering configurations.

Figure.5: Raman spectra for the cleaved sample at region II for different scattering configurations. The inset shows the SiH_2 stretching region.

Figure 6: PL spectra at region I for $E_i//E_e$ (F) and $E_i \perp E_e$ (A) configurations.

Figure 7: PL spectra at region II for $E_i//E_e$ (F) and $E_i \perp E_e$ (A) configurations.

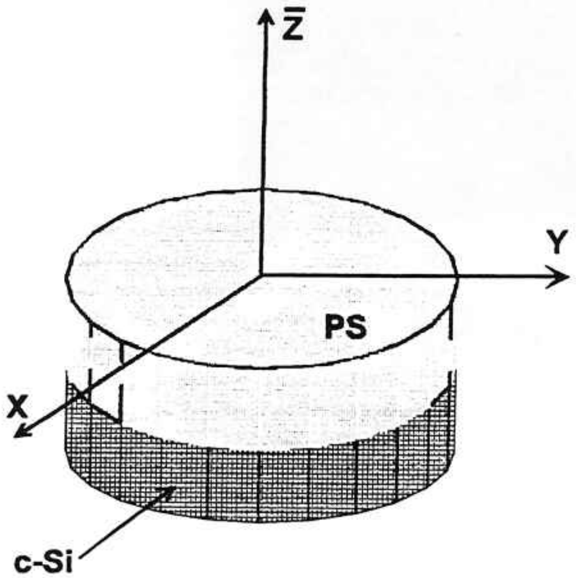

(a) Uncleaved sample

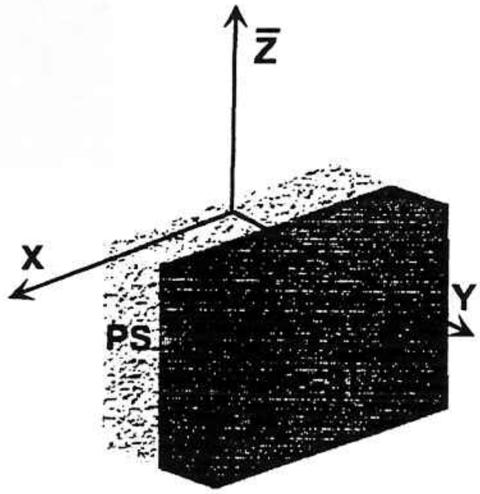

(b) Cleaved sample

Figure 1.

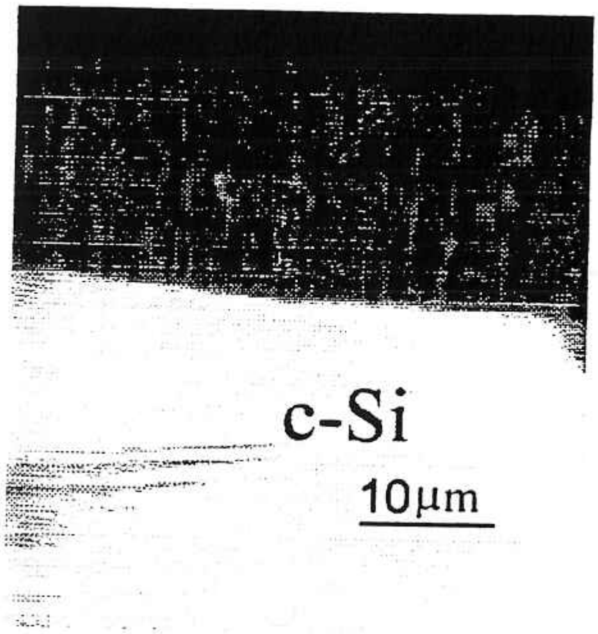

Figure 2.

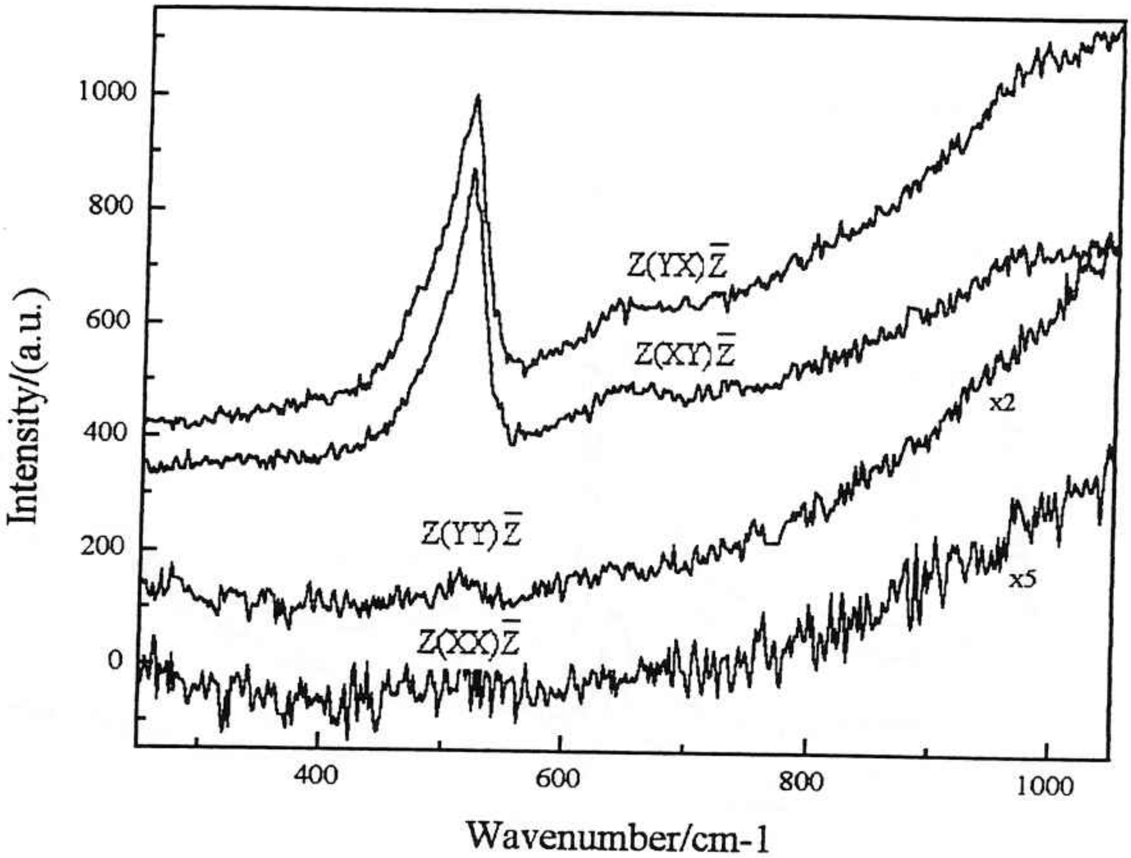
1000
800
600
400
200
0
Intensity/(a.u.)
400
600
800
1000
Wavenumber/cm-1
Z(YX)Z̄
Z(XY)Z̄
Z(YY)Z̄
Z(XX)Z̄
x2
x5

Figure 3.

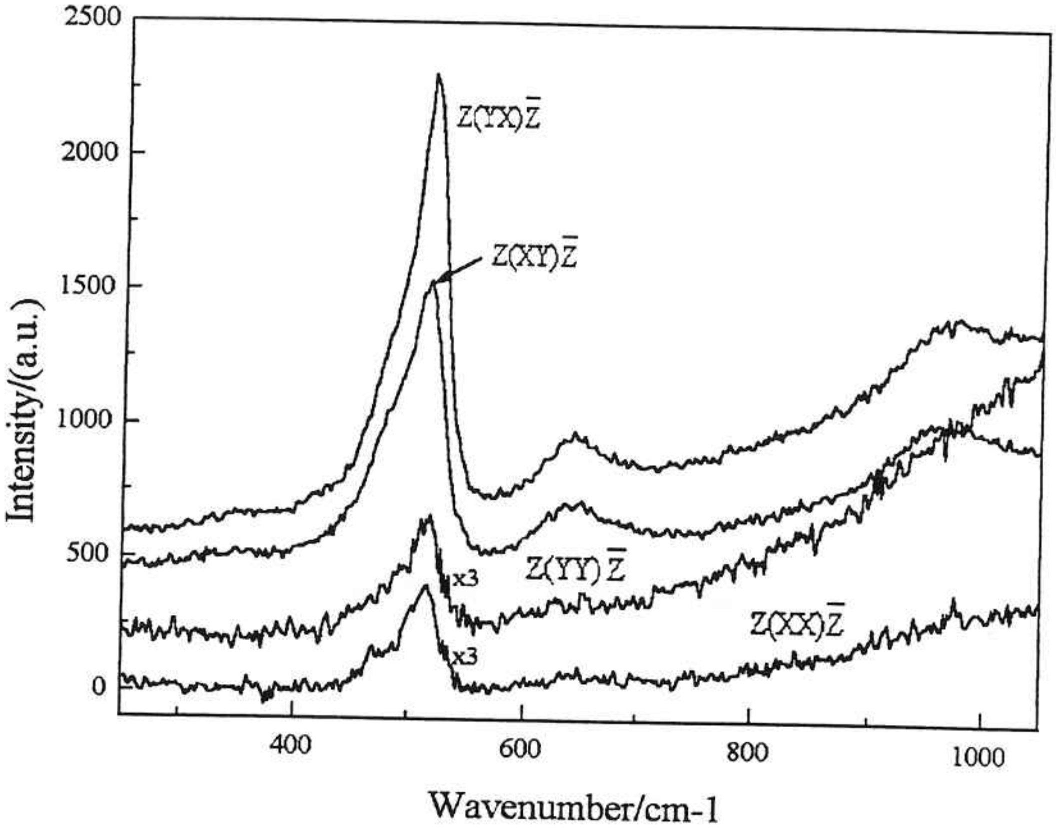

2500
2000
1500
1000
500
0
Intensity/(a.u.)
400
600
800
1000
Wavenumber/cm-1
Z(YX)$\bar{Z}$
Z(XY)$\bar{Z}$
Z(YY)$\bar{Z}$
Z(XX)$\bar{Z}$
x3
x3

Figure 4.

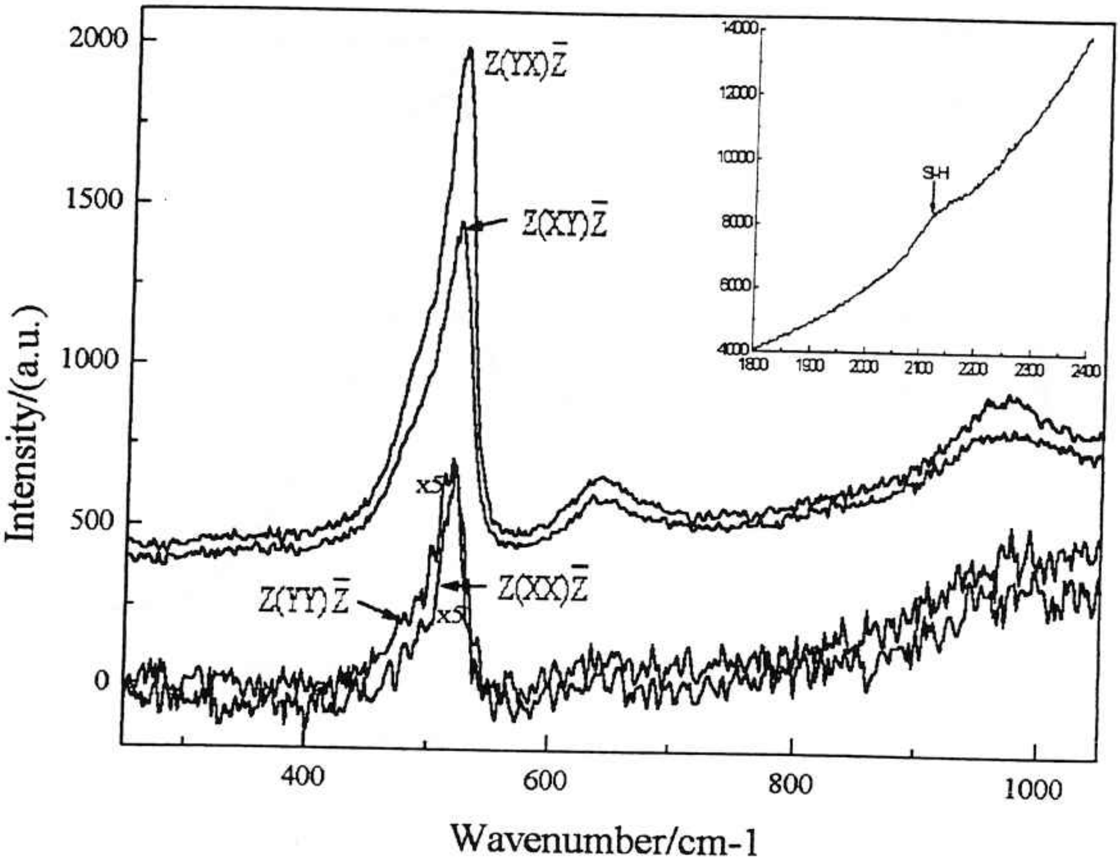
2000
1500
1000
500
0
Intensity/(a.u.)
400
600
800
1000
Wavenumber/cm-1
Z(YX)Z̄
Z(XY)Z̄
Z(YY)Z̄
Z(XX)Z̄
x5
x5
Si-H
14000
12000
10000
8000
6000
4000
1800
1900
2000
2100
2200
2300
2400

Figure 5.

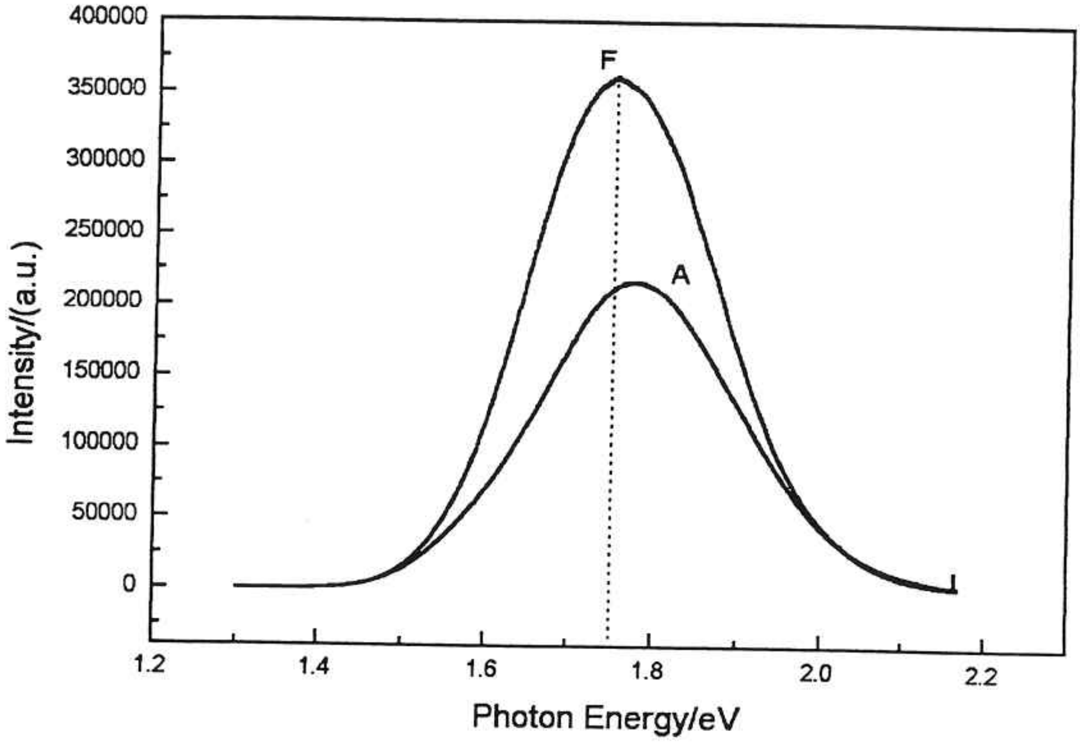
400000
350000
300000
250000
200000
150000
100000
50000
0
Intensity/(a.u.)
F
A
1.2
1.4
1.6
1.8
2.0
2.2
Photon Energy/eV

Figure 6.

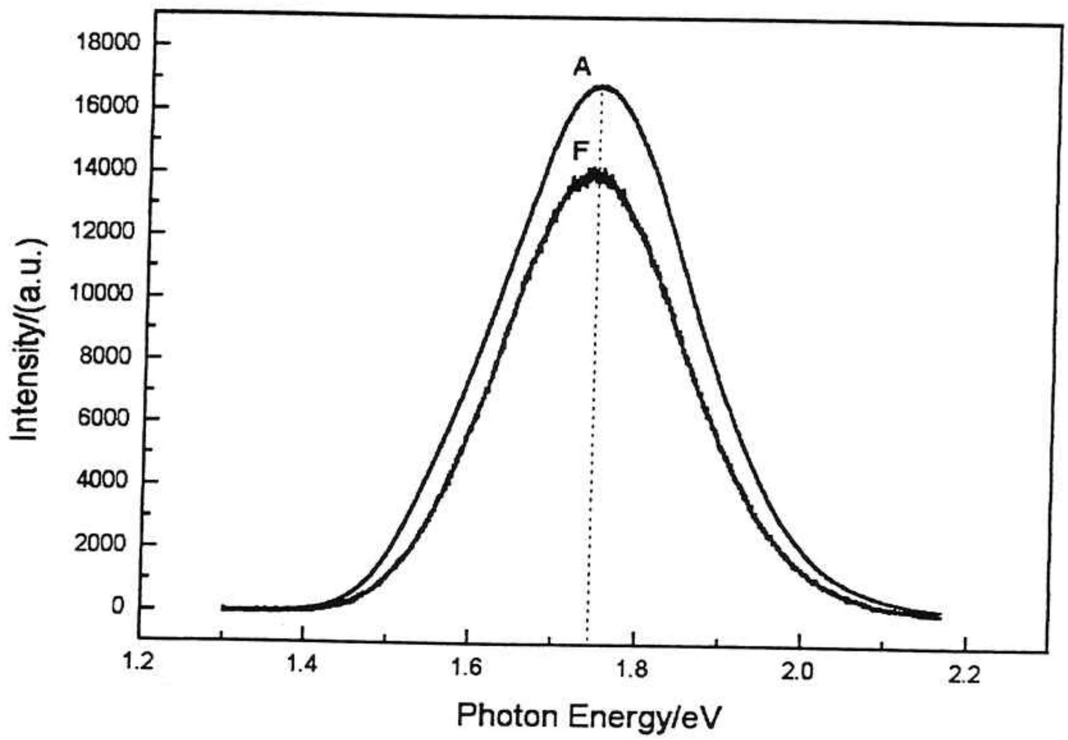

A
F
18000
16000
14000
12000
10000
8000
6000
4000
2000
0
Intensity/(a.u.)
1.2
1.4
1.6
1.8
2.0
2.2
Photon Energy/eV

Figure 7.

BOLETINS TÉCNICOS - TEXTOS PUBLICADOS

BT/PEE/9301 - Oscilador a HEMT - 10 GHz - FÁTIMA S. CORRERA, EDMAR CAMARGO

T/PEE/9302 - Representação Senoidal da Voz através dos Polos do Filtro Preditor - MARCELO B. JOAQUIM, NORMONDS ALENS

BT/PEE/9303 - Blindagens por Grades Condutoras: Cálculo do Campo Próximo - LUIZ CEZAR TRINTINALIA, ANTONIO ROBERTO PANICALI

BT/PEE/9304 - Sistema de Otimização e Controle de Produção em Minas de Pequeno e Médio Porte - TSEN CHUNG KANG, VITOR MARQUES PINTO LEITE

BT/PEE/9401 - Determinação das Frases de Aplicação Forense para o projeto NESPER e Tese de Mestrado IME/94, com Base em Estudos Fonéticos - MARCONI DOS REIS BEZERRA, EUVALDO F. CABRAL JUNIOR

BT/PEE/9402 - Implementação e Teste de uma Rede Neural Artificial do TIpo KSON (Kohonen Self-Organizing Network) com Entradas Bidimensionais - MARCELO YASSUNORI MATUDA, EUVALDO F. CABRAL JR.

BT/PEE/9403 - Transformada de Walsh e Haar Aplicadas no Processamento de Voz - ALEXANDRE AUGUSTO OTTATI NOGUEIRA, THIAGO ANTONIO GRANDI DE TOLOSA, EUVALDO F. CABRAL JÚNIOR

BT/PEE/9404 - Aplicação de Redes Neurais ao Problema de Reconhecimento de Padrões por um Sonar Ativo - ALEXANDRE RIBEIRO MORRONE, CRISTINA COELHO DE ABREU, EDUARDO KOITI KIUKAWA, EUVALDO F. CABRAL JR.

BT/PEE/9405 - Tudo que se Precisa Saber sobre a Prática da FFT - Transformada Rápida de Fourier (Inclui Software) - ROGÉRIO CASAGRANDE, EUVALDO F. CABRAL JR.

BT/PEE/9406 - A Survey on Speech Enhancement Techniques of Interest to Speaker Recognition - CELSO S. KURASHIMA, EUVALDO F. CABRAL JR.

BT/PEE/9407 - Identificação de Pulsos Decádicos em Linhas Telefônicas - ANTONIO P. TIMOSZCZUK, MÁRCIO A. MATHIAS, EUVALDO F. CABRAL JR.

BT/PEE/9408 - Implementação e Teste de Filtros do Tipo Adaptativo e ©Notchª para a Remoção de Interferência de 60 Hz em Sinais de Eletrocardiograma - FLÁVIO ANTÔNIO MENEGOLA, JOSÉ AUGUSTO DE MATTOS, JOSÉ GOMES G. FILHO, SIDNEY SILVA VIANA, EUVALDO F. CABRAL JR.

BT/PEE/9409 - Compressão de Sinais de Voz utilizando Transformadas de Karhunen-Loève, Fourier e Hadamard - IVAN LUIS VIEIRA, LUIZ FERNANDO STEIN WETZEL, EUVALDO F. CABRAL JR.

BT/PEE/9410 - ©Ray Tracingª Paralelo - EDUARDO TOLEDO SANTOS, JOÃO ANTONIO ZUFFO

BT/PEE/9411 - Implementação de uma Ferramenta Posicionador para ©Gate-Arraysª Tipo Mar de Portas - JORGE W. PERLAZA PRADO, WILHELMUS A. M. VAN NOIJE

BT/PEE/9412 - Tudo que se Precisa Saber Sobre a Teoria da FFT - Transformada Rápida de Fourier - FÁBIO LUÍS ROMÃO, REINALDO SILVEIRA, ROGÉRIO CASAGRANDE, EUVALDO CABRAL JR.

BT/PEE/9413 - Análise do Ruído Sonoro em uma Sala de Aquisição de Amostras de Som com Microcomputador - FÁBIO LUÍS ROMÃO, REINALDO SILVEIRA, EUVALDO CABRAL JR.

BT/PEE/9414 - Cor: Aspectos Relevantes para Visualização de Dados - SÍLVIA DELGADO OLABARRIAGA

BT/PEE/9415 - Projeto de Filtros Digitais IIR com Fase Aproximadamente Linear Utilizando Redução de Ordem - IVAN F. J. RODRIGUES, MAX GERKEN

BT/PEE/9416 - GERAFILTRO: Sistema para Projeto Automático de Filtros Digitais ©IIRª (da especificação em alto nível ao leiaute do ©ASICª) - RICARDO PIRES, JOSÉ VIEIRA DO VALE NETO

BT/PEE/9417 - Redes Neurais Artificiais Aplicadas à Identificação de Pulsos Decádicos em Linhas Telefônicas - ANTONIO P. TIMOSZCZUK, EUVALDO F. CABRAL JR.

BT/PEE/9501 - Estudo Comparativo de Métodos de Cálculo da Frequência Fundamental - MARCOS COSTA HUNOLD, EUVALDO F. CABRAL JR.

BT/PEE/9502 - Combinando Técnicas de Redes Neurais Artificiais e Informações de Excitação no Reconhecimento Automático do Locutor - ANDRÉ BORDIN MAGNI, EUVALDO F. CABRAL JR.

BT/PEE/9503 - Utilização de Redes Neurais Artificiais para Detecção e Identificação de Falhas em Circuitos - MÁRCIO YUKIO TERUYA, ROBERTO AMILTON BERNARDES SÓRIA, EUVALDO CABRAL JR.

BT/PEE/9504 - Uso de Redes Neurais Artiificiais no Reconhecimento de Locutores no Domínio Temporal - BENEDITO JOSÉ BARRETO FONSECA JÚNIOR, EUVALDO CABRAL JÚNIOR

BT/PEE/9505 - Projeto de Filtros Passivos e Ativos em Técnicas de Circuitos Integrados de Microondas - DAVID VIVEIROS JÚNIOR, DENISE CONSONNI

BT/PEE/9506 - Uma Análise de Clustering para as Frases de Projeto NESPER - RONALDO OLIVEIRA MESSINA, EUVALDO F. CABRAL JR.

BT/PEE/9507 - Controle com Estrutura Variável e Modos Deslizantes - Um Estudo para Aplicação em Controle Carga-frequência da Geração - JOSE PAULO F. GARCIA, JOCELYN FREITAS BENNATON

BT/PEE/9508 - Recuperação das Margens de Ganho e de Fase para Sistemas de Fase Não Mínima por Realimentação da Saída - MARCO H. TERRA, VITOR M. P. LEITE

BT/PEE/9509 - Sistema de Inspeção Óptica de Dispositivos Bi-Dimensionais - CASIMIRO DE ALMEIDA BARRETO, PEDRO LUÍS PRÓSPERO SANCHEZ

T/PEE/9510 - Sistema de Partículas Uma Poderosa Técnica de Animação em Computação Gráfica - RENATO CURTO RODRIGUES, JOÃO ANTÔNIO ZUFFO

BT/PEE/9511- Efeito de Ruídos em Sinais de Voz Visualizados em Trajetórias Neurais de Kohonen - CELSO S. KURASHIMA, EUVALDO F. CABRAL JR.

BT/PEE/9601 - "Um Reconhecedor de Sinais Sonoros Utilizando LVQ" - ALEXANDRE TORNICE, EUVALDO CABRAL JR.

BT/PEE/9602 - "Coleção Artificial Neural Networks: Uma Visão Geral dos Sistemas Neurais Artificais de Stephen Grossberg" - CHIU HSIUNG HUANG

BT/PEE/9603 - "Reactively-Sputtered TiN Formation Using a RF Magnetron System"- SÉRGIO PAULO AMARAL OSÓRIO, LUIZ SÉRGIO ZASNICOFF

BT/PEE/9604 - Aspectos em Tradução de Linguagens Naturais Através de Redes Neurais Artificiais - CARLOS EDUARDO DANTAS DE MENEZES, EUVALDO F. CABRAL JR.

BT/PEE/9605 - Implementação de Blocos Passa-Tudo Utilizando Realimentação de Erro - SÉRGIO JOSÉ CARNEIRO LEÃO, MAX GERKEN

BT/PEE/9606 - Coleção SANN group Redes Neurais Artificiais: A Rede Neural de Sakoe - ANDRÉ BORDIN MAGNI, EUVALDO F. CABRAL JR.

BT/PEE/9607 - Coleção SANN group Redes Neurais Artificiais: A Rede Neural de Steinbuch - ROBERTO AMILTON BERNARDES SÓRIA, EUVALDO F. CABRAL JR.

BT/PEE/9608 - Desenvolvimento de uma Estrutura de Duplo Nível de Metal para a Confecção de Interconexões em Circuitos Integrados - JOSÉ AUGUSTO DE ALENCAR PEREIRA, LUIZ CARLOS MOLINA TORRES

BT/PEE/9609 - Determinação de Parâmetros de Processo para Fotomáscara "Balzers" Utilizando Gerador de Padrões - JORGE SEKI, MEGUMI SAITO

BT/PEE/9610 - Um Ambiente para Desenvolvimento de Sistemas Distribuídos - PEDRO F. ROSA, JOÃO A. ZUFFO

BT/PEE/9611 - Interpretações Teóricas do Funcionamento Cerebelar: Uma Revisão - MARCUS FRAGA VIEIRA, ANDRÉ FÁBIO KOHN

BT/PEE/9612 - Marcapasso Cardíaco Temporário Microcontrolado de Demanda e Baixo Consumo - FLAVIO ANTONIO MENEGOLA, JOSÉ CARLOS TEIXEIRA DE BARROS MORAES

BT/PEE/9613 - Um Sistema de Planejamento de Ação Baseado em Casos para uma Célula Flexível de Manufatura - RICARDO LUÍS DE FREITAS, MÁRCIO RILLO

BT/PEE/9614 - Aplicações do Boundary-Scan para o Teste de Módulos Multichip - ROBERTO C. COSSI JR., JOSÉ ROBERTO DE A. AMAZONAS

BT/PEE/9615 - A 2.488 Gb/s GaAs 1:4/1:16 Demultiplexer IC with Skip Circuit for Sonet STS-12/48 Systems - TAUFIK ABRÃO, FATIMA S. CORRERA

BT/PEE/9616 - Uma Contribuição para a Construção de Algoritmos em Projetos de Redes - ALLAN DE SOUZA, JOSÉ ROBERTO CASTILHO PIQUEIRA

BT/PEE/9617 - Análise Crítica dos Métodos de Medição do Intervalo QT do Eletrocardiograma - SÍDNEY DA SILVA VIANA, JOSÉ CARLOS TEIXEIRA DE BARROS MORAES

BT/PEE/9618 - Deposição e Caracterização de Filmes de SiO2 Crescidos pela Técnica de PECVD a Baixa Temperatura - MARCO ALAYO CHÁVEZ, INÉS PEREYRA

BT/PEE/9619 - PARSTOOL: Uma Ferramenta de Auxílio à Simulação de Sistemas Paralelos - LI KUAN CHING, LIRIA MATSUMOTO SATO

BT/PEE/9620 - Análise de um Método de Otimização por Malha no Treinamento de Robôs - OLÍMPIO MURILO CAPELI, JOSÉ CARLOS T. B. MORAES, SADAO ISOTANI

BT/PEE/9701 - Identification of Unstable Mechanical Systems - ROBERTO MOURA SALES, ANSELMO BITTAR, MICHAEL PORSCH, LAÉRCIO LUCCHESI

BT/PEE/9702 - Analysis of the Subthreshold Slope Transition Region in SOI nMOSFET - VICTOR SONNENBERG, JOÃO ANTONIO MARTINO

BT/PEE/9703 - Introduction of the SOI MOSFET Dimensions in the High-Temperature Leakage Drain Current Model - MARCELO BELLODI, JOÃO ANTONIO MARTINO, DENIS FLANDRE

BT/PEE/9704 - Controle de Largura de Banda Dinâmica para Transmissões Multicast para Redes de Alta Velocidade - SANG SOON LEE, SERGIO TAKEO KOFUJI

BT/PEE/9705 - Uma Modificação Proposta para o Controle Preditivo Generalizado com Filtro de Kalman - JAIME QUINTERO R., OSWALDO L. V. COSTA

BT/PEE/9706 - Aplicações de Redes Neurais em Previsões Financeiras - OLÍMPIO MURILO CAPELI, EUVALDO F. CABRAL JR.

BT/PEE/9707 - Sistema Microcontrolado, Multicanal e Portátil para Estimulação Neuromuscular Funcional - ROGÉRIO QUIARIM ZARZA, JOSÉ CARLOS TEIXEIRA DE BARROS MORAES

BT/PEE/9708 - Requisitos para o Mapeamento Tecnológico em Projetos de Microeletrônica - LUCIANO DE OLIVEIRA CORRÊA DE BRITO, JOSÉ ROBERTO DE ALMEIDA AMAZONAS

BT/PEE/9709 - Sistemas PRMA com Dados Acoplados - JOSÉ AUGUSTO DE LIMA, PAUL JEAN ETIENNE JESZENSKY

BT/PEE/9710 - Algoritmos Genéticos (AG's) para a Otimização de Controladores Nebulosos - JULIO CESAR CEBALLOS AYA, OSWALDO L. V. COSTA

BT/PEE/9711 - Um Estudo Sobre a Redução de Ruídos em Sinais Caóticos - ERNANE JOSÉ XAVIER COSTA, EUVALDO F. CABRAL JR.

BT/PEE/9712 - Geradores não Lineares de Sequência para uso em Sistemas Spread Spectrum - ANGEL ANTONIO GONZALEZ MARTINEZ, PAUL JEAN ETIENNE JESZENSZKY

BT/PEE/9713 - Modelamento Físico do Sistema Heteroestrutura - Metal - CECÍLIA WETTERLE RODRIGUES, MEGUMI SAITO

BT/PEE/9714 - Tensões Induzidas em Linhas Aéreas por Descargas Atmosféricas Indiretas - Modelagem e Aplicação ao Cálculo de Interrupções - ALEXANDRE PIANTINI, JORGE M. JANISZEWSKI

BT/PEE/9715 - RECMAP - Uma Ferramenta para Otimização em Síntese de Alto Nível Baseada em Reconhecimento Funcional e Mapeamento de Componentes - ANDRÉ GERHARD, JOSÉ VIEIRA DO VALE NETO

BT/PEE/9716 - Estudo da Sinterização de Contatos Al/Ti por Recozimento Térmico Rápido Visando a Aplicação em Circuitos Integrados - ANGELO EDUARDO BATTISTINI MARQUES, ROGÉRIO FURLAN

BT/PEE/9717 - Mixed H2/H- Control of Discrete-Time Markovian Jump Linear Systems - OSWALDO L. V. COSTA, RICARDO P. MARQUES

BT/PEE/9718 - Aluminium Etching with CCl4-N2 Plasmas - ANGELA MAKIE MAKAZAWA, PATRICK VERDONCK

BT/PEE/9719 - O Uso de Resistes Amplificados Quimicamente e de Sililação em Litrografia por Feixe de Elétrons - ANTONIO C. SEABRA, PATRICK B. VERDONCK

BT/PEE/9720 - Implementação de um Simulador de um Circuito Neuro-Medular que Atua no Controle da Força Motora - LUIZ JURANDIR SIMÕES DE ARAÚJO,ANDRÉ FÁBIO KOHN

BT/PEE/9721 - Avaliação das Características Físico-Químicas e Elétricas de Filmes de SiO2 Depositados por PECVD a Patir da Reação entre O2 e TEOS - ALVARO ROMANELLI CARDOSO E CLAUS MARTIN HASENACK

BT/PEE/9722 - Controle e Simulação Dinâmica de Colunas de Destilação: Aplicação Prática em uma Coluna com Refluxo por Gravidade

BT/PEE/9723 - Circuitos de Portas Lógicas Primitivas Implementados a Partir de uma Classe de Lógicas Paraconsistentes Anotadas - JOÃO INÁCIO DA SILVA FILHO, JAIR MINORO ABE, PEDRO LUÍS PRÓSPERO SANCHEZ

BT/PEE/9724 - Lattice Heating and Energy Balance Consideration on the I-V Characteristics of Submicrometer Thin-Film Fully Depleted SOI NMOS Devices - CLAUDIA BRUNETTI, NELSON L. A. BRAGA, LUIZ S. ZASNICOFF

BT/PEE/9725 - Identificação de um Processo de Neutralização de pH via Redes Neurais - SILVIO FLABOREA, CLAUDIO GARCIA

BT/PEE/9726 - Uma Estratégia de Migração de Sistemas de Telefonia Movél com Tecnologia AMPS para a Tecnologia CDMA - RONALD LUÍS CLARKSON EISNER, PAUL JEAN ETIENNE JESZENSKY

BT/PEE/9727 - Controle de pH Usando Conceitos de Invariantes de Reações e Geometria Diferencial - OSCAR A. ZANABARIA S., CLAUDIO GARCIA

BT/PEE/9728 - Estudo da Influência dos Parâmetros de Recozimento Térmico Rápido na Morfologia dos Filmes de TiSi2 Formados e sua Correlação com a Tensão Mecânica - SILVANA GASPAROTTO DE SOUZA, ARMANDO ANTONIO MARIA LAGANÁ, SEBASTIÃO GOMES DOS SANTOS FILHO

BT/PEE/9729 - Analysis of Silicon Surface Microirregularities by LASER Ligght Scattering - JOSÉ CÂNDIDO DE SOUSA FILHO, SEBASTIÃO GOMES DOS SANTOS FILHO

BT/PEE/9730 - Wavelets in Music Analysis and Synthesis: Timbres Analysis and Perspectives - REGIS ROSSI ALVES FARIA, RUGGERO ANDREA RUSCHIONI, JOÃO ANTONIO ZUFFO

BT/PEE/9731 - Estudo de Efeitos Mútuos da Distribuição de Corrente em Condutores - AUGUSTO CARLOS PAVÃO, JORGE MIECZYSLAW JANISZEWSKI

BT/PEE/9801 - Equivalência entre a Semântica da Lógica de Transações e a Semântica de sua Implementação Prolog - PAULO E. SANTOS, FLÁVIO S. C. DA SILVA

BT/PEE/9802 - Nash Game in Mixed H2/Hoo Control Theory a Convex Optimization Approach- HELENICE OLIVEIRA FLORENTINO, ROBERTO MOURA SALES

BT/PEE/9803 - Text-Independent Speaker Recognition Using Vector Quantization and Gaussian Mixture Models - THOMAS E. FILGUEIRAS Fº., RONALDO O. MESSINA E EUVALDO F. CABRAL JR.

BT/PEE/9804 - Elementos Piezoresistivos para Sensores de Pressão com Tecnologia CMOS - LUIZ ANTONIO RASIA, E. C. RODRIGUEZ

BT/PEE/9805 - Automação do Processo de Casamento de Impedância em Sistemas de Aquecimento por Microondas - J. C. DE SOUZA, J. T. SENISE, V. C. PARRO, F. M. PAIT

BT/PEE/9806 - Considerações para o Projeto de Células de Memória SI com Transístores HEMT - JAIME H. LASSO, EDGAR CHARRY R.

BT/PEE/9807 - Covariance Controller with Structure Constraint and Closed Loop H Bound - ANTÔNIO CARLOS DE LIMA, ROBERTO MOURA SALES

BT/PEE/9808 - Controle Unidimensional de Objetos: Uma Aplicação Prática em Fresadora Automática - MÁRCIO A. F. MURATORE, OSWALDO L. V. COSTA

BT/PEE/9809 - Redes Neurais com Retardos Temporais Aplicadas ao Reconhecimento Automático do Locutor - ROGÉRIO CASAGRANDE, EUVALDO F. CABRAL JR.

BT/PEE/9810 - Topological Computation and Voluntary Control - HENRIQUE SCHÜTZER DEL NERO, JOSÉ ROBERTO CASTILHO PIQUEIRA, ALFREDO PORTINARI MARANCA

BT/PEE/9811 - Casamento de Impedância em Guia de Onda Retangular Utilizando como Variável Medida a Potência Refletida - J. C. DE SOUZA JR., J. T. SENISE

BT/PEE/9812 - Applied Surface Science - RONALDO D. MANSANO, PATRICK VERDONCK, HOMERO S. MACIEL

BT/PEE/9813 - Contribuição ao Estudo da Morfologia da Superfície e da Interface do Siliceto de Titânio Formado sobre Si (100) Empregando a Técnica de Microscopia de Força Atômica (AFM) - N. M. HASAN, A. A. M. LAGANÁ, S. G. SANTOS FILHO

BT/PEE/9814 - Estudo Experimental da Tensão Mecânica em Filmes Finos de Cobre Obtidos por Evaporação ou Deposição Eletroquímica Espontânea - A. I. HASHIMOTO, S. G. FILHO

BT/PEE/9815 - Controle Híbrido de Manipuladores Robóticos - WEBER ALLEGRINI, JOSÉ JAIME DA CRUZ

BT/PEE/9816 - Entropia Informacional e Cronobiologia - ANA AMÉLIA BENEDITO SILVA, JOSÉ ROBERTO CASTILHO PIQUEIRA

BT/PEE/9817 - Estabilidade de Lyapunov e Controle de Atitude - FERNANDO SOUSA, FREITAS JÚNIOR, PAULO SÉRGIO PEREIRA DA SILVA

BT/PEE/9818 - Projeto de um Conversor de Frequências Resistivo em Tecnologia MMIC - CLÁUDIA C. A. APARÍCIO, DENISE CONSONNI

BT/PEE/9819 - Estudo de Sensibilidade de um Sistema de Modulação Digital via Simulação - RONALDO DI MAURO, LUIZ ANTONIO BACCALÁ

BT/PEE/9820 - Engenharia do Conhecimento Aplicada ao Conhecimento Aplicada ao Domínio de Gerenciamento de Falhas em Redes de Comunicação: Uma Abordagem Baseada em Modelo - MARILZA ANTUNES DE LEMOS, MARCIO RILLO

BT/PEE/9821 - Uma Biblioteca de Métodos de Resolução de Problemas de Planejamento para Fornecer Apoio à Aquisição de Conhecimento - LELIANE NUNES DE BARROS, MARCIO RILLO

BT/PEE/9822 - Um Estudo de Técnicas de Aprendizado por Reforço Livre de Modelo - Aplicação ao Pêndulo Invertido - SÉRGIO RIBEIRO AUGUSTO, ADEMAR FERREIRA

BT/PEE/9823 - Identificação de Sistemas Dinâmicos com Redes Neurais - FRANCISCO CARLOS PONS, CLÁUDIO GARCIA

BT/PEE/9824 - Comparison between Single and Double Langmuir Probe Techniques for Analysis of Inductively Coupled Plamas - RAUL M. DE CASTRO, GIUSEPPE A. CIRINO, PATRICK VERDONCK, HOMERO S. MACIEL, MARCOS MASSI, MARCELO B. PISANI, RONALDO D. MANSANO

BT/PEE/9825 - DECMEF: Um Sistema de Decomposição Aplicada à Síntese de Máquinas de Estados Finitos - CARLOS HUMBERTO LLANOS QUINTERO, MARIUS STRUM

BT/PEE/9826 - Controladores Preditivos Através de Desigualdade Matriciais Lineares - RENATO C. BARÃO, RICARDO P. MARQUES, OSWALDO L. V. COSTA

BT/PEE/9827 - Parametrization of all H2 Optimal Output Feedback Controllers - JOÃO YOSHIYUKI ISHIHARA, ROBERTO MOURA SALES

BT/PEE/9901 – Digital Equalization Using Time Delay Neural Network (TDNN) – MARIO ANDRÉS VERGARA ESCOBAR, EUVALDO F. CABRAL JR.

BT/PEE/9902 – Simulação e Análise Estrutural do Modelo de Deposição da Publicação ICRP 66 – JOAQUIM CARLOS SANCHES CARDOSO, JOSÉ CARLOS T. DE BARROS MOARAES

BT/PEE/9903 – Modelamento e Ajuste por Regra Sub-Ótica de Maximização da Informação da Mútua de um Sistema Reconhecedor de Palavras Isoladas, Independente do Falante, para Ambientes Adversos, com Redundância de Informação – MÁRIO MINAMI, IVANDRO SANCHES

BT/PEE/9904 – Modelagem Matemática e Controle Multivariável do Tanque de Contato Empregado no Processo de Lixiviação dos Minerais Niquelíferos – DANIEL GUZMÁN DEL RÍO, CLAUDIO GARCIA

BT/PEE/9905 – Avaliação de Transdutores para Análise Metabólica Humana – HENRIQUE TAKACHI MORIYA, JOSÉ CARLOS T. DE BARROS MORAES

BT/PEE/9906 – Estudo da Aplicação do Método TLM-2D à Análise de Campos Eletromagnéticos - MARCO ANTONIO MATHIAS, JORGE M. JANISZEWSKI

BT/PEE/9907 – Comportamento Transitório de Campos Eletromagnéticos em Meios Condutores: Simulação Computacional Eficiente por Diferenças Finitas no Domínio do Tempo – ALEXANDRE AUGUSTO OTTATI NOGUEIRA, JORGE MIECZYSLAW JANISZEWSKI

BT/PEE/9908 – H_2 and H_∞ Control for Maglev Vehicles – ANSELMO BITTAR, ROBERTO MOURA SALES

BT/PEE/9909 – Amplificador Distribuído em GaAs – 1 a 17 GHz – CRISTIANE FERREIRA DE ARAÚJO, FATIMA SALETE CORRERA

BT/PEE/9910 – Modelo Não-Linear de MESFET para Simulação de Amplificadores de Alta Eficiência – ANTONIO SANDRO VERRI, FATIMA SALETE CORRERA

BT/PEE/9911 – Projeto de um Sistema de Propulsão e Levitação Magnética com Dois Graus de Liberdade – ALEXANDRE BRINCALEPE, FELIPE MIGUEL PAIT

BT/PEE/9912 – A New Technique to Obtain the MOS Gate Oxide Thickness and Electric Breakdown Field Distributions From Fowler-Nordheim Tunneling Current – WILLIAN AURÉLIO NOGUEIRA, SEBASTIÃO GOMES DOS SANTOS FILHO